Unsupervised Land Cover/Land Use Classification Using PolSAR Imagery Based on Scattering Similarity

Qiang Chen, Gangyao Kuang, *Member, IEEE*, Jonathan Li, *Senior Member, IEEE*, Lichun Sui, and Diangang Li

***Abstract*—This paper presents a new unsupervised land cover/land use classification scheme using polarimetric synthetic aperture radar (PolSAR) imagery based on polarimetric scattering similarity. Compared with the H/alpha classification scheme based on a dominant "average" scattering mechanism, the proposed scheme has such advantages as the following: 1) The major scattering mechanism represents a target scattering in the low-entropy case; 2) it also represents both the major and minor scattering mechanisms in the medium-entropy case; and 3) all the scattering mechanisms in the high-entropy case can be represented. The major and minor scattering mechanisms have been identified automatically based on the relative magnitude of multiple-scattering similarities. The canonical scattering corresponding to maximum scattering similarity is regarded as the major scattering mechanism. The result obtained using the National Aeronautics and Space Administration/Jet Propulsion Laboratory's AIRSAR L-band PolSAR imagery reveals that the proposed scheme is more effective as compared to the existing models and promises to increase the accuracy of the classification and interpretation.**

***Index Terms*—Land cover/land use, radar polarimetry, scattering similarity, synthetic aperture radar (SAR), unsupervised classification.**

I. Introduction

SPACEBORNE synthetic aperture radar (SAR) imagery has long been used as an appropriate and effective data source for land cover/land use mapping due to its advantages. However, many of the reported studies have been carried out based on the availability of single-frequency and single-polarization SAR images (e.g., C-band VV ERS-1/ERS-2 and HH RADARSAT-1). Land cover/land use features cannot be significantly separated based on a single-band backscattering signature alone. Research showed that land cover/land use classification using single-frequency or single-polarization SAR data is not sufficiently accurate [1]. With the availability of L-band ALOS PALSAR, C-band RADARSAT-2, and X-band TerraSAR-X, high-spatial-resolution, multifrequency, multipolarization, or fully polarimetric SAR (PolSAR) images have proven very useful for various applications including land cover/land use mapping [2].

PolSAR image classification has been an interesting research topic in the geoscience and remote sensing community. In the past decade, classification algorithms have been proposed based on probability distributions of PolSAR data [3]–[7]. For a one-look case, PolSAR data are represented by a Sinclair matrix [2]. It was assumed that the Sinclair matrix has a complex Gaussian distribution [8]. Kong *et al.* [3] derived a distance measure for maximum-likelihood classification. Yueh *et al.* [4] extended this approach for normalized PolSAR data classification. van Zyl and Burnette [6] further expanded it by iteratively applying *a priori* probability of the classes. For a multilook case, PolSAR data can be expressed in the form of a covariance or coherency matrix [2]. This has a complex Wishart distribution [8]. Lee *et al.* [7] developed a supervised algorithm based on this distribution. Furthermore, Ferro-Famil *et al.* [9], [10] have extended these classification algorithms to multifrequency and PolSAR interferometry data.

The idea of alternative classification approach is to classify PolSAR images based on the inherent characteristics of physical scattering mechanisms [11]–[15]. This kind of classification algorithm has an advantage of providing scattering type identification. Many researchers have proposed target decomposition (TD) theorems in radar polarimetry [16]–[26] to make a better understanding of the scattering process. Up to now, TD has become a standard tool for analyzing physical scattering mechanisms. TD can be categorized into two main types. They are coherent and incoherent decomposition. Natural targets are usually irregularly distributed, and only incoherent decomposition is considered here. There are three kinds of representation to target scattering based on incoherent decomposition. They are as follows: 1) to model target scattering with a certain scattering mechanism that can be extracted

Manuscript received January 21, 2011; revised December 10, 2011 and March 26, 2012; accepted May 11, 2012. Date of publication September 7, 2012; date of current version February 21, 2013.

Q. Chen is with the School of Electronic Science and Engineering, National University of Defense Technology, Changsha 410073, China and also with the 93502 Unit, People's Liberation Army, Hohhot 010000, China (e-mail: cq9822090@163.com).

G. Kuang is with the Remote Sensing Information Processing Laboratory, National University of Defense Technology, Changsha 410073, China (e-mail: kuangyeats@hotmail.com).

J. Li is with the Key Laboratory of Underwater Acoustic Communication and Marine Information Technology, Ministry of Education, and the School of Information Science and Engineering, Xiamen University, Xiamen 361005, China, and also with the Laboratory for GeoSpatial Technology and Remote Sensing, Department of Geography and Environmental Management, University of Waterloo, Waterloo, ON N2L 3G1, Canada (e-mail: junli@xmu.edu.cn; junli@uwaterloo.ca).

L. Sui is with the State Key Laboratory of Astronautic Dynamics, Xi'an 710043, China, and also with the School of Geology Engineering and Geomatics, Chang'an University, Xi'an 710064, China (e-mail: sui1011@chd.edu.cn).

D. Li is with the 93502 Unit, People's Liberation Army, Hohhot 010000, China.

Color versions of one or more of the figures in this paper are available online at http://ieeexplore.ieee.org.

Digital Object Identifier 10.1109/TGRS.2012.2205389

TABLE I
PROPOSED PARAMETERS CORRESPONDING TO A CANONICAL SCATTERER

Canonical scatterer	Pauli vectors	Polarimetric scattering similarity
Metallic sphere or flat plate	$\begin{bmatrix}\sqrt{2} & 0 & 0\end{bmatrix}^T$	$\frac{T_{11}}{T_{11}+T_{22}+T_{33}}$
Dihedral oriented at 0°	$\begin{bmatrix}0 & \sqrt{2} & 0\end{bmatrix}^T$	$\frac{T_{22}}{T_{11}+T_{22}+T_{33}}$
Dihedral oriented at 45°	$\begin{bmatrix}0 & 0 & \sqrt{2}\end{bmatrix}^T$	$\frac{T_{33}}{T_{11}+T_{22}+T_{33}}$
Line target	$\begin{bmatrix}1/\sqrt{2} & 1/\sqrt{2} & 0\end{bmatrix}^T$	$\frac{T_{11}+T_{22}+2\,\mathrm{Re}(T_{12})}{2(T_{11}+T_{22}+T_{33})}$
Right helix	$\begin{bmatrix}0 & 1/\sqrt{2} & -i/\sqrt{2}\end{bmatrix}^T$	$\frac{T_{22}+T_{33}+2\,\mathrm{Im}(T_{23})}{2(T_{11}+T_{22}+T_{33})}$
Left helix	$\begin{bmatrix}0 & 1/\sqrt{2} & i/\sqrt{2}\end{bmatrix}^T$	$\frac{T_{22}+T_{33}-2\,\mathrm{Im}(T_{23})}{2(T_{11}+T_{22}+T_{33})}$

by Huynen decomposition [16]; 2) to use a major scattering mechanism, which can be extracted by model-based TD [18]–[25]; and 3) to use an average scattering mechanism. Among them, the one based on the average scattering mechanism has been the most widely used classification algorithm applied to classify PolSAR images. Assuming that there is always a dominant "average" scattering mechanism [12], then a three-symbol Bernoulli process can be used to extract the parameters of average component (i.e., average alpha angle and entropy). The average alpha angle characterizes the average scattering mechanism, and the entropy is a measure of randomness of scattering mechanisms. These two key parameters will be used to construct a classification scheme later. However, the assumption of dominant "average" scattering mechanism is not always reasonable. Certainly, when the scattering randomness is low, the major scattering mechanism is dominant, and it can be used to denote the scattering of a distributed target. However, when the scattering randomness is very high, particularly equal to one, then target scattering is completely stochastic, and no scattering mechanism can be used to represent this kind of target scattering. To resolve this problem, a novel classification scheme has been proposed in this paper.

Based on a special correlation coefficient, a novel approach to extracting scattering features was proposed in [27]. In this study, a parameter is defined to measure the similarity degree between two scattering matrices. Then, it has been used to extract similarity parameters to canonical scatterings. These kinds of scattering features not only have fine properties (i.e., independent of the spans of the scattering matrices or the scatterer orientation angles) but also can be extracted efficiently. Now, they have been widely used to terrain classification and detection. However, this parameter cannot be applied straightly for the incoherent case because the scattering process of the distributed target is represented by a coherence matrix and no equivalent scattering matrix exists for its coherence matrix. In order to overcome this deficiency, a novel polarimetric scattering similarity is defined and has been used to extract the scattering features of a distributed target [28]. This paper discusses its extending possibilities and application in PolSAR image classification.

This paper has been organized as follows. In Section II, polarimetric scattering similarity and relationships with alpha angle and entropy are defined. Section III details the deficiency of the H/alpha classification scheme and proposes a polarimetric-scattering-similarity-based classification scheme. In Section IV, the results are discussed and compared with those of the H/alpha classification scheme. Section V contains concluding remarks.

II. POLARIMETRIC SCATTERING SIMILARITY

A. Definition of Polarimetric Scattering Similarity

To overcome the deficiencies of the parameter introduced by Yang *et al.* [27], a novel parameter has been proposed to measure the scattering similarity between a random scatterer and a canonical scatterer [28]. Let $\vec{k}$ be the Pauli target feature vector of a canonical scatterer and $[T]$ be the coherency matrix of an arbitrary random scatterer. Then, polarimetric scattering similarity can be defined as

$$rss = \frac{\vec{k}^{*T}[T]\vec{k}}{\mathrm{trace}(\vec{k}\vec{k}^{*T}) \times \mathrm{trace}\,([T])} \tag{1}$$

where the superscript * denotes complex conjugate, $\mathrm{trace}(\bullet)$ is the trace operation of a matrix, and rss is considered to be limited to the range [0, 1]. The larger the rss is, the more similar the scatterings of the two targets are. The limitation is that the scatterings of the two targets are the same when $rss = 1$.

With this novel parameter rss, some characteristics of a distributed target can be extracted. Table I lists the polarimetric scattering similarity parameters corresponding to several canonical scatterers, such as sphere, dihedral, and helix. In Table I, T_{ij}, with $i, j = 1, 2, 3$, represents the elements of $[T]$, and $\mathrm{Re}(\bullet)$ and $\mathrm{Im}(\bullet)$ denote the real and imaginary parts of a complex number, respectively. This table reveals that the sum of the polarimetric scattering similarity parameters corresponding to the sphere and the dihedrals oriented at 0° and 45° is equal to one. The same scenario would be seen when the polarimetric scattering similarity parameters correspond to the sphere, right helix, and left helix.

Furthermore, if the elements of the coherency matrix are denoted by Huynen parameters, then the polarimetric scattering similarity parameters corresponding to the sphere and the dihedrals oriented at 0° and 45° can be interpreted as the contributive ratios of surface scattering. This also interprets double-bounce scattering and volume scattering to the total backscattering, respectively [28]. Moreover, their sum is equal to one, which means that the scattering of any target can be regarded as the contribution of these three aforementioned scatterings.

B. Relationship Between Polarimetric Scattering Similarity and Alpha Angle

Consider that the coherency matrix is decomposed with its eigenvectors $\vec{e}_i$, where $i = 1, 2, 3$, and eigenvalues λ_i, where $i = 1, 2, 3$, and the eigenvectors are expressed as follows:

$$\vec{e}_i = e^{j\xi_i}[\cos\alpha_i \quad \sin\alpha_i\cos\beta_i e^{j\sigma_i} \quad \sin\alpha_i\sin\beta_i e^{j\gamma_i}]^{\mathrm{T}} \quad (2)$$

where α_i is the scattering angle, β is the target orientation angle, ξ is the absolute phase, and σ and γ are the relative target phase angles. Then, the surface scattering similarity can be rewritten as a function of α_i and p_i

$$rss_s = p_1\cos^2\alpha_1 + p_2\cos^2\alpha_2 + p_3\cos^2\alpha_3 \quad (3)$$

where $p_i = \lambda_i/(\lambda_1+\lambda_2+\lambda_3)$. Obviously, the rss_s definition can be considered very close to the definition of the mean alpha angle $\overline{\alpha}$. Hence, rss_s can be expressed as a function of $\overline{\alpha}$ for the following three extreme cases.

1) When a target has only one scattering mechanism or is deterministic

$$rss_s = \cos^2\overline{\alpha}. \quad (4)$$

2) When a target has multiscattering mechanisms and one is surface scattering

$$rss_s = 1 - 2\overline{\alpha}/\pi. \quad (5)$$

3) When a target has two kinds of scattering mechanisms whose Pauli vectors are not orthogonal to the one of surface scattering, then

$$rss_s = \frac{2\cos^2\left(\frac{\alpha\sin\left(\frac{2}{\pi}\right)}{2}\right)}{\alpha\sin\left(\frac{2}{\pi}\right)-\pi}\left(\overline{\alpha}-\frac{\pi}{2}\right), \qquad \frac{1}{2}\alpha\sin\left(\frac{2}{\pi}\right)\le\overline{\alpha}\le\frac{\pi}{2}. \quad (6)$$

The lines determined by (4)–(6) are shown in Fig. 1 as real, dashed, and dashed–dotted lines, respectively. These lines form an envelope, and all the points are situated in the feasible areas, which means that these lines give the borderlines for all possible combinations of rss_s and $\overline{\alpha}$.

C. Relationships Between Polarimetric Scattering Similarity and Entropy

In the same way, rss_s is related to entropy H. For example, when $H = 1$, $rss_s = 1/3$. On the other hand, when $H = 0$, the full range of possible rss_s is accessed. It understands that the possible values of rss_s decrease as the entropy increases and the range of these possible values can be determined by p_3 and p_1.

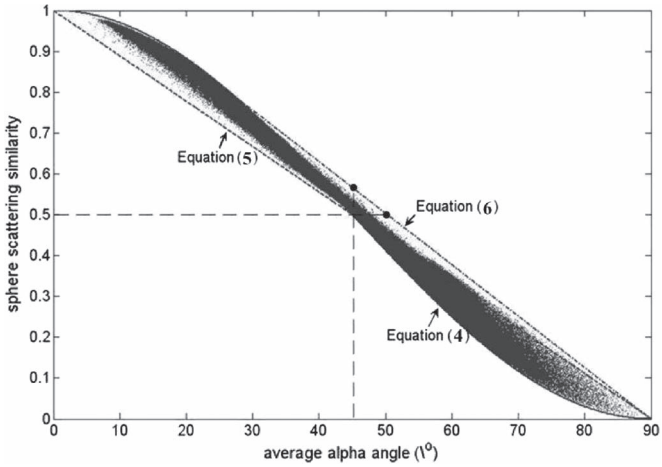

Fig. 1. Relation between surface scattering similarity and average alpha angle. The dots represent the scatter plot between parameter values calculated for the image. The lines show extreme values of the parameters.

With orthogonality between the eigenvectors of the coherency matrix and the properties of the polarimetric scattering similarity, it can be deduced that $\cos^2\alpha_1 + \cos^2\alpha_2 + \cos^2\alpha_3 = 1$. Thus

$$\begin{aligned} p_1 - rss_s &= p_1 - \sum_{i=1}^{3} p_i\cos^2\alpha_i \\ &= (p_1-p_2)\cos^2\alpha_2 + (p_1-p_3)\cos^2\alpha_3 \\ &\ge 0 \end{aligned} \quad (7)$$

$$\begin{aligned} rss_s - p_3 &= \sum_{i=1}^{3} p_i\cos^2\alpha_i - p_3 \\ &= (p_1-p_3)\cos^2\alpha_1 + (p_2-p_3)\cos^2\alpha_2 \\ &\ge 0. \end{aligned} \quad (8)$$

Obviously, the possible value of rss_s is between p_3 and p_1.

Furthermore, p_3 and p_1 can be determined by the entropy. Considering that $p_1 + p_2 + p_3 = 1$, the extreme relationships between p_1 (or p_3) and the entropy can be expressed as

$$H \le -p_1\log_3(p_1) - (1-p_1)\log_3\left(\frac{(1-p_1)}{2}\right), \quad \frac{1}{3} \le p_1 \le 1 \quad (9)$$

$$H \ge -p_1\log_3(p_1) - (1-p_1)\log_3(1-p_1), \quad 0 \le 1-p_1 \le 0.5; \quad p_3 = 0 \quad (10)$$

$$H \ge -p_3\log_3(p_3) - (1-p_3)\log_3\left(\frac{(1-p_3)}{2}\right), \quad 0 \le p_3 \le \frac{1}{3}. \quad (11)$$

The curves determined by (9)–(11) are shown in Fig. 2 as real lines. Obviously, these curves form a closed area together with

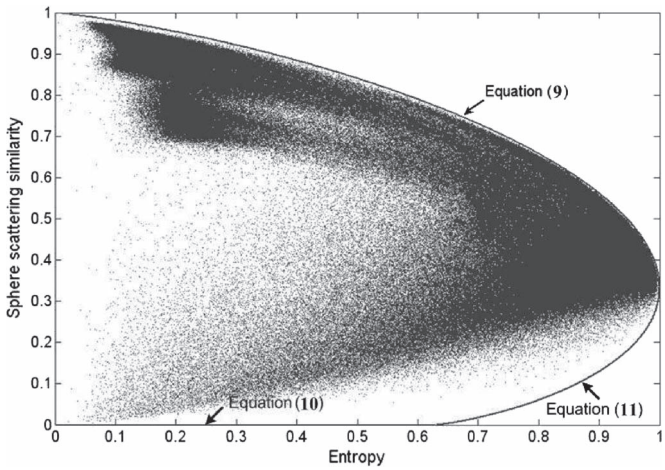

Fig. 2. Relation between surface scattering similarity and entropy. The dots represent the scatter plot between parameter values calculated for the image. The lines show extreme values of the parameters.

a line $H = 0$, and all the points are situated in this feasible area. This means that the curves give the borderlines for all possible combinations of rss_s and H. The shape of the feasible area is formed by all possible combinations of rss_s and H and is further similar to that of the feasible area formed by all possible combinations of $\overline{\alpha}$ and H. This also means that an analyst can consider a 2-D $H-rss_s$ classification space instead of an $H-\overline{\alpha}$ classification space.

III. Classification With Polarimetric Scattering Similarity

A. Deficiency of H/Alpha Classification Scheme

As mentioned in Section I, the H/alpha classification scheme has been widely applied in the present literatures, but it assumed that there is a dominant "average" scattering mechanism and it is not justified. This paper tries to prove it as follows.

If $\vec{e}_i$ is regarded as a certain scattering mechanism and p_i represents its relative importance with respect to the total scattered power, then the major scattering mechanism can be determined by the maximum of p_i, with $i = 1, 2, 3$, and its scattering randomness is expressed as [2]

$$H = -\sum_{i=1}^{3} p_i \log_3(p_i). \tag{12}$$

The entropy is limited to [0, 1]. The larger the H is, the higher the scattering randomness is. Considering that $p_1 + p_2 + p_3 = 1$, then entropy can be rewritten as

$$\begin{aligned} H = &-(p_1 \log_3(p_1) + p_3 \log_3(p_3)) \\ &-(1 - p_1 - p_3)\log_3(1 - p_1 - p_3). \end{aligned} \tag{13}$$

Let $p_1 \geq p_2 \geq p_3$ be without loss of generality; we can obtain

$$1-2p_3 \geq p_1 \geq \frac{(1-p_3)}{2} \quad \text{or} \quad \frac{(1-p_1)}{2} \geq p_3 \geq \max(1-2p_1, 0). \tag{14}$$

With (13) and (14), Fig. 3 shows the contour plot of the entropy in the (p_1, p_3) plane, in which the entropy is not a unique function of the eigenvalues and all possible values of entropy are located in a triangular area. The triangular area has been divided into 21 subareas as shown in Fig. 3.

The corresponding ranges of p_i and H are listed in Table II, which shows the following.

1) When the entropy is very low such as in subarea 1, p_1 is absolutely bigger than p_2 or p_3. The contribution of the major scattering mechanism to the total backscattering is so big that the contributions of other scattering mechanisms can be neglected.
2) When the entropy is very high such as in subarea 21, the ranges of p_1, p_2, and p_3 are so close. No scattering mechanism is dominant, and the contributions of all scattering mechanisms are nearly equal.
3) When the entropy is medium, the values of p_1 and p_2 may be nearly equal. When p_3 is so small, its corresponding contribution to the total backscattering can be neglected such as in subarea 11.
4) When the entropy is still medium, the values of p_2 and p_3 may be nearly equal, and their corresponding contributions to the total backscattering cannot be neglected such as in subarea 16.

The aforementioned discussions indicate that representation with a major scattering mechanism to target scattering is not always reasonable, particularly when the entropy is very high.

B. Classification Scheme With Polarimetric Scattering Similarity

To overcome the deficiency mentioned in Section III-A, this study has proposed a novel method to represent target scattering. First, target scattering is divided into three cases: low entropy, medium entropy, and high entropy. For the low-entropy case, the major scattering mechanism is used to denote target scattering because its contribution to the total backscattering is absolutely dominant. For the medium-entropy case, the contributive ratio (e.g., p_2) of minor scattering mechanisms is also significant. Therefore, the major and minor scattering mechanisms are used together to denote target scattering. For the high-entropy case, the contributive ratios of all scattering mechanisms are nearly close, and it has no meaning to identifying a scattering mechanism.

Obviously, the identification of scattering mechanisms is the key stone of this new method. As the parameter defined by (1) measures the degree of scattering similarity between a distributed scatterer and a canonical scatterer, it can be used naturally to identify scattering mechanisms. The basic idea is to compare target scattering with multiple canonical scatterings. The canonical scattering corresponding to the maximum scattering similarity has been designated as the major scattering mechanism. The canonical scattering corresponding to the minor maximum scattering similarity has also been designated as the minor scattering mechanism.

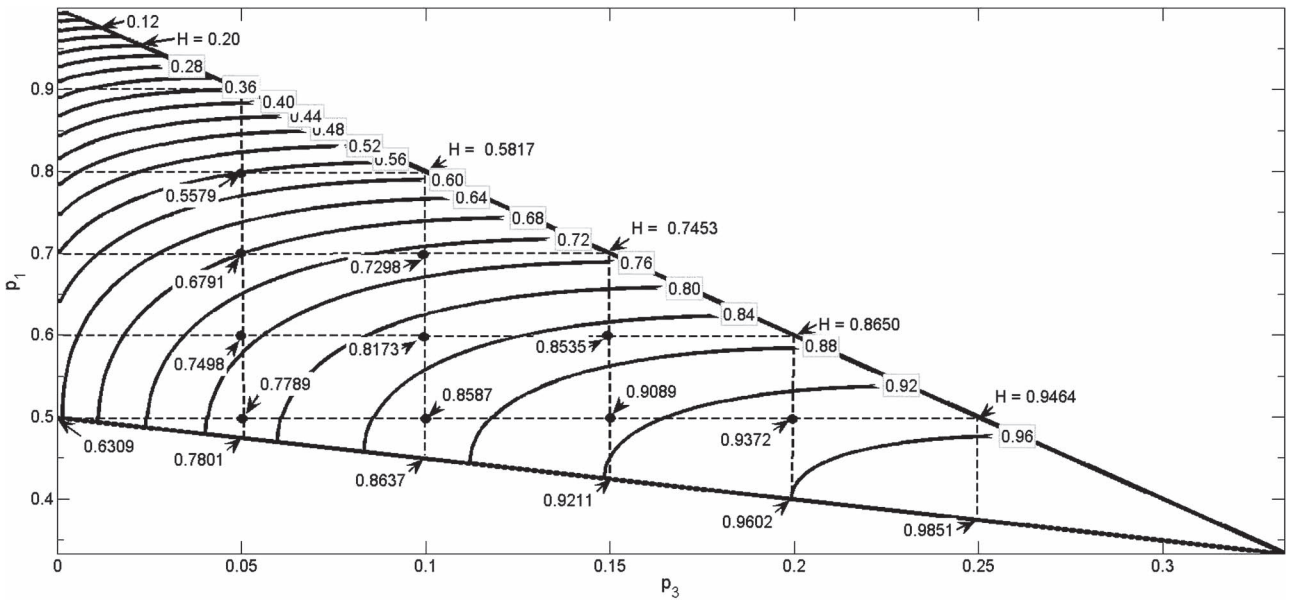

Fig. 3. General behavior of the entropy as a function of p_1 and p_3.

TABLE II
VALUE RANGES OF p_1, p_2, p_3, AND H CORRESPOND TO SUBAREAS

Area	p_1	p_2	p_3	H	Area	p_1	p_2	p_3	H
1	0.9~1	0~0.1	0~0.05	0~0.3590	12	0.7~0.8	0.1~0.2	0.1~0.15	0.5817~0.7453
2	0.8~0.9	0.05~0.2	0~0.05	0.2959~0.5579	13	0.6~0.7	0.15~0.3	0.1~0.15	0.7298~0.8535
3	0.7~0.8	0.15~0.3	0~0.05	0.4555~0.6791	14	0.5~0.6	0.25~0.4	0.1~0.15	0.8173~0.9089
4	**0.6~0.7**	**0.25~0.4**	**0~0.05**	0.5560~0.7498	15	0.425~0.5	0.35~0.45	0.1~0.15	0.8587~0.9211
5	**0.5~0.6**	**0.35~0.5**	**0~0.05**	0.6126~0.7789	16	0.6~0.7	0.15~0.25	0.15~0.2	0.7453~0.8650
6	**0.475~0.5**	**0.45~0.5**	**0~0.05**	0.6309~0.7801	17	0.5~0.6	0.2~0.35	0.15~0.2	0.8535~0.9372
7	0.8~0.90	0.05~0.15	0.05~0.1	0.3590~0.5817	18	0.4~0.5	0.3~0.425	0.15~0.2	0.9089~0.9602
8	0.7~0.8	0.1~0.25	0.05~0.1	0.5579~0.7298	19	0.5~0.6	0.2~0.3	0.2~0.25	0.8650~0.9464
9	**0.6~0.7**	**0.2~0.35**	**0.05~0.1**	0.6791~0.8173	20	0.375~0.5	0.25~0.4	0.2~0.25	0.9372~0.9851
10	**0.5~0.6**	**0.3~0.45**	**0.05~0.1**	0.7498~0.8587	21	0.333~0.5	0.25~0.333	0.25~0.333	0.9464~1
11	**0.45~0.5**	**0.4~0.475**	**0.05~0.1**	0.7789~0.8637					

When applying this idea, the following principles have to be put into account.

1) The selected canonical targets should be based on the physics of radar scattering and not a purely mathematical construct. Thus, it matches well with the general polarimetric scattering behavior of terrain.
2) The polarimetric scattering similarity between selected canonical targets should be small as much as possible.
3) The number of selected canonical targets should be moderate. Certainly, the more the canonical targets selected, the more fine the classification that will be achieved.

However, this will bring heavy computational burden. After studying deeply polarimetric scattering similarities in Table I, it has been found that only the surface scattering similarity, double-bounce scattering similarity, and volume scattering similarity are accorded with the aforementioned principles. The scattering mechanism of a sphere is referred to as a single- or odd-bounce scattering. The scattering mechanism of a dihedral oriented at 0° is referred to as a double- or even-bounce scattering, since the polarization of the returned wave is mirrored with respect to the one of the incident wave. The scattering mechanism of a diplane oriented at 45° is referred to as those scatterers that are able to return the orthogonal polarization. One of the best examples is the volume scattering produced by forest canopy. The more important thing is that these three scattering similarities can be regarded as the contribution ratios of these three canonical scatterings to target total backscattering. Therefore, any target scatterings can be regarded as the superposition of these three canonical scatterings.

Based on the above analysis, Fig. 4 shows the polarimetric-scattering-similarity-based classification scheme. The entire unsupervised classification procedure is as follows.

1) If the original data do not have sufficient averaging in the number of looks, polarimetric speckle filtering, e.g., refined Lee filter [29], is performed for PolSAR data. All

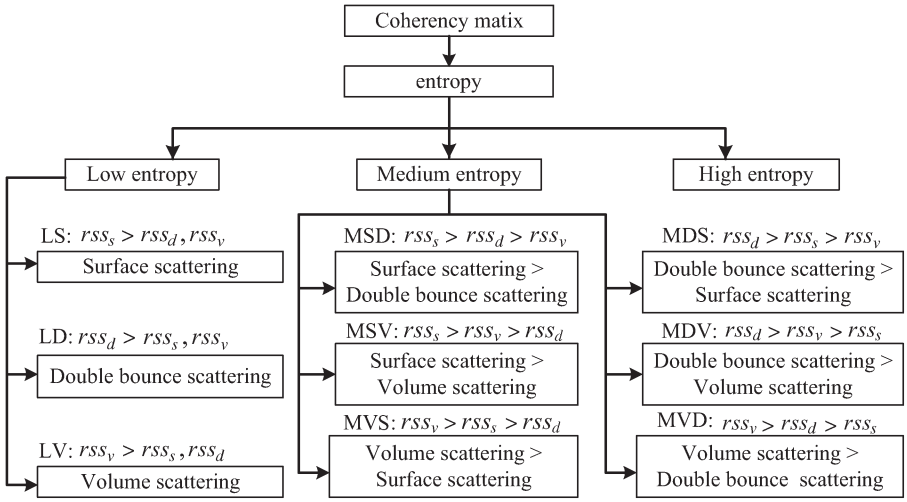

Fig. 4. Classification scheme with polarimetric scattering similarity and entropy.

elements of the 3 × 3 coherency matrix should be filtered simultaneously.

2) Compute entropy, surface scattering similarity, double-bounce scattering similarity, and volume scattering similarity.
3) Label each pixel by entropy as one of the three scattering categories: low entropy, medium entropy, and high entropy.
4) Divide the pixels of each category into more small clusters.
   a) For the low-entropy category, label each pixel by the relative magnitude of surface scattering similarity, double-bounce scattering similarity, and volume scattering similarity as one of the three scattering categories: low-entropy surface scattering (LS), low-entropy double-bounce scattering (LD), and low-entropy volume scattering (LV).
   b) For the medium-entropy category, label each pixel by the relative magnitude of surface scattering similarity, double-bounce scattering similarity, and volume scattering similarity as one of the six scattering categories: medium-entropy surface–double scattering (MSD), medium-entropy double–surface scattering (MDS), medium-entropy surface–volume scattering (MSV), medium-entropy volume–surface scattering (MVS), medium-entropy volume–double scattering (MVD), and medium-entropy double–volume scattering (MDV). MSD means that the contribution of surface scattering is larger than that of double-bounce scattering for the medium-entropy case. The other abbreviations have similar meanings.

It should be pointed out that the proposed scheme is not the only one and the study offers this scheme merely to illustrate our classification strategy based on polarimetric scattering similarities. After all, Table I does not list all polarimetric scattering similarities. Then, the boundary between low entropy and medium entropy or between medium entropy and high entropy is decided artificially according to application demands.

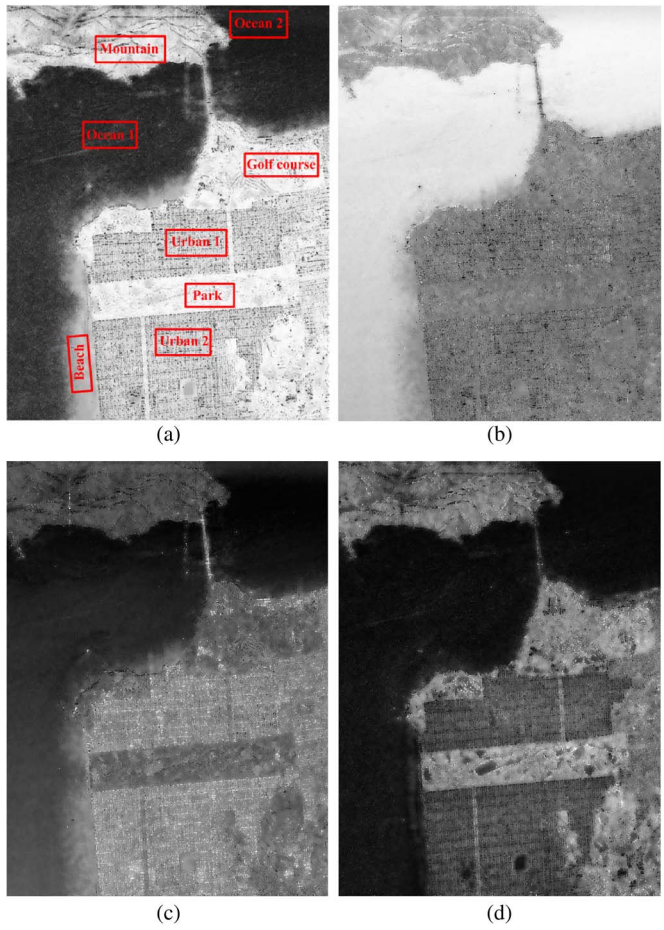

Fig. 5. Entropy and scattering similarity images of the study area: (a) Entropy, (b) surface scattering similarity, (c) double-bounce scattering similarity, and (d) volume scattering similarity.

IV. Experimental Results and Discussions

A. Classification Results With the Proposed Scheme

A 10-m-spatial-resolution four-look L-band PolSAR image with the radar incidence angles ranging from 5° to 60° and an image size of 900 × 700 pixels acquired by the National

TABLE III
COMPARISON BETWEEN SCATTERING FEATURES OF DIFFERENT LAND COVER/LAND USE TYPES

Terrain	Water1	Water2	Urban1	Urban2	Mountain	Beach	Park	Golf course
rss_s	0.8861	0.9325	0.3654	0.3655	0.5360	0.5160	0.4219	0.4489
rss_d	0.0870	0.0482	0.4892	0.5085	0.2431	0.4430	0.3293	0.2987
rss_v	0.0269	0.0193	0.1454	0.1260	0.2209	0.0409	0.2489	0.2524
rss_l	0.2626	0.3558	0.4443	0.4558	0.3979	0.5153	0.3270	0.3604
rss_{hl}	0.0399	0.0223	0.3038	0.2969	0.2428	0.2223	0.2873	0.2822
rss_{hr}	0.0740	0.0452	0.3308	0.3376	0.2212	0.2617	0.2908	0.2690
H	0.1871	0.1247	0.7753	0.7647	0.8577	0.7303	0.9309	0.9185
$\overline{\alpha}$	18.0511	12.8438	55.4510	55.5034	42.9829	43.9154	50.3186	48.6999
p_1	0.9603	0.9644	0.6152	0.6406	0.5968	0.5369	0.4590	0.4750
p_2	0.0245	0.0143	0.2684	0.2867	0.1641	0.3354	0.2989	0.3030
p_3	0.0168	0.0067	0.0660	0.0511	0.0924	0.0305	0.2088	0.1996
α_1	9.1807	8.6448	70.0547	66.6405	10.8583	39.2998	33.0655	24.4208
α_2	78.7502	83.3730	26.2824	28.6905	82.3705	51.0368	67.3040	70.8297
α_3	75.7646	84.5850	76.7350	77.1070	83.0633	86.4134	69.7300	77.7961

Aeronautics and Space Administration/Jet Propulsion Laboratory's AIRSAR over San Francisco, CA, was used in this study to test the proposed classification scheme. This scene contains several land cover/land use types, including water (sea), beach, urban, mountain, and vegetation that have a variety of distinctive scattering mechanisms.

To possess enough averaging, a speckle filter was applied. The entropy image calculated from the speckle-filtered image is shown in Fig. 5(a). The scattering randomness is clearly shown with large values in vegetation areas, e.g., park and golf course, small values in ocean areas, and medium values in urban areas. The surface scattering similarity, double-bounce scattering similarity, and volume scattering similarity are also computed from the speckle-filtered image, and their images are shown in Fig. 5(b)–(d). These scattering similarity images depict ocean areas with the largest values of surface scattering similarity, urban areas with the largest values of double-bounce scattering similarity, and vegetation areas with biggish values of volume scattering similarity.

This study also computes the average alpha angle, the maximum eigenvalue ratio, and the scattering similarities to the dipole, left helix, and right helix, respectively. Eight land cover classes are shown in Fig. 5(a). Table III lists the values of the aforementioned parameters, from which we can find the following: 1) The difference between rss_{hl} and $rss_{h\gamma}$ is very small for all the above terrains; 2) the values of rss_l corresponding to all the terrains are nearly equal; 3) for low-entropy ocean areas, rss_s is larger than 0.75; 4) for the median-entropy city area, rss_d is slightly larger than rss_s; and 5) for high-entropy vegetation areas, rss_s, rss_d, and rss_ν are close. This means that the preceding three scattering similarities have poor performance to distinguish different terrains, but it is not the case for rss_s, rss_d, and rss_ν.

With the entropy and scattering similarities to the sphere and the dihedrals oriented at 0° and 45°, the proposed scheme was applied to the PolSAR test image. Fig. 6 shows the statistical histogram of the entropy image. The boundary between low entropy and medium entropy or between medium entropy and high entropy is determined by the inflection point of the curve, such as points A and B shown in Fig. 6.

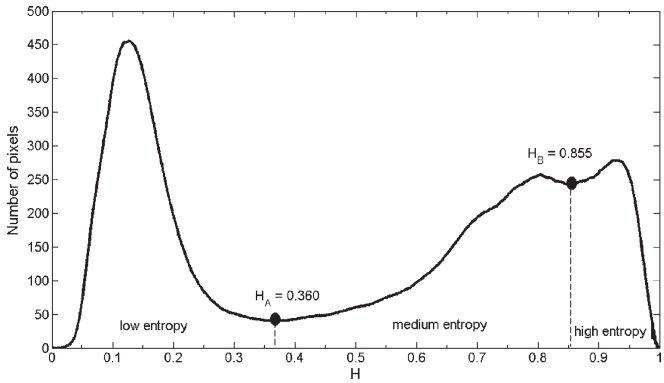

Fig. 6. Statistical histogram of the entropy image of the study area.

B. Comparison With H/Alpha Classification Results

Fig. 7 shows the classification results obtained using (a) the proposed classification scheme and (b) the H/alpha classification scheme. The classified land cover/land use types are represented using different false colors. Information related with each class can be used to infer target scattering mechanisms and terrains with different scattering characteristics. This also helps detect the objects in the image. In Fig. 7(b), the abbreviations of HM, MV, and LS denote high-entropy multiple scattering, medium-entropy vegetation scattering, and low-entropy surface scattering, respectively. Other abbreviations are analogously defined. By comparing the two classification maps (a) and (b) in Fig. 7, it can be concluded that more detailed information in the complex urban area can be detected by the proposed scheme than the H/alpha scheme. For example, some

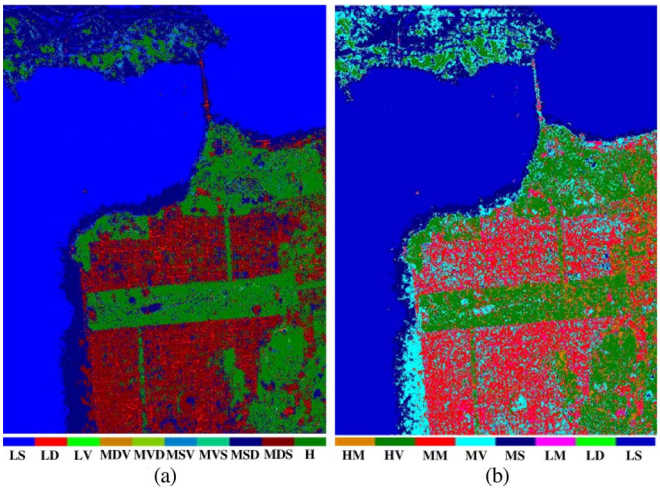

Fig. 7. Classification results of the study area using (a) our classification scheme and (b) the H/alpha classification scheme.

ambiguous areas (e.g., golf courses and roads) in Fig. 7(b) are well discriminated in Fig. 7(a). Pixels in coastal areas are mainly classified as MV in Fig. 7(b) but as MSD in Fig. 7(a). Since coastal areas are commonly composed of sands, blocks, and water, therefore, surface scattering is the major scattering contribution to target backscattering (see Table II). The contribution ratio of double-bounce scattering is also biggish. Therefore, this study believes that the classification results are more reliable than the H/alpha classification results. Moreover, few pixels in urban, mountain, and Golden Gate Bridge are also mistakenly classified as MV by the H/alpha scheme but are correctly classified as MSD by the proposed scheme.

The misclassification by the H/alpha classification scheme may be due to the obscure definition of average alpha angle $\overline{\alpha}$. $\overline{\alpha}$ is defined as a weighted sum of eigenvector angles. In coastal areas, the contribution of surface scattering is close to that of double-bounce scattering, i.e., $\overline{\alpha}$ is close to $\pi/4$. Thus, these areas are classified as MS by the H/alpha classification scheme. However, this is not the case for the proposed classification scheme because the scattering type is assigned by the relative magnitude of scattering similarities automatically. These two scattering mechanisms can be separated.

Furthermore, in the proposed classification scheme, $\overline{\alpha}$ is defined as a weighted sum of eigenvector angles that makes the physical meaning of its classification result obscure. The coastal areas are classified based on MSD. This infers that surface scattering is the major scattering mechanism. This also reveals that the double-bounce scattering is the minor scattering mechanism and the contributions of these two scattering mechanisms are almost equal.

V. Conclusion

This paper has presented a new unsupervised classification scheme based on scattering similarity using PolSAR imagery. The pixels have been divided into three scattering categories, namely, low entropy, medium entropy, and high entropy. Then, the pixels of the low-entropy category have been subdivided based on the major scattering mechanism. The pixels of the medium-entropy category were subdivided based on the major and minor scattering mechanisms. The major and minor scattering mechanisms have been identified according to the relative magnitude of multiscattering similarities corresponding to sphere, dihedral, etc. For example, the canonical scattering corresponding to the maximum scattering similarity is regarded as the major scattering mechanism. Compared with the H/alpha scheme, the proposed classification scheme can determine borderlines of the scattering type automatically. The result obtained from AIRSAR L-band PolSAR imagery has demonstrated that the proposed classification scheme has better performance for land cover/land use classification and mapping than the existing H/alpha classification scheme.

Acknowledgment

The authors would like to thank the National Aeronautics and Space Administration's Jet Propulsion Laboratory for providing the AIRSAR L-band polarimetric synthetic aperture radar data. The authors would also like to thank the anonymous reviewers for their valuable comments.

References

[1] J. S. Lee, M. R. Grunes, and E. Pottier, "Quantitative comparison of classification capability: Fully polarimetric versus dual and single-polarization SAR," *IEEE Trans. Geosci. Remote Sens.*, vol. 39, no. 11, pp. 2343–2351, Nov. 2001.

[2] J. S. Lee and E. Pottier, *Polarimetric Radar Imaging: From Basics to Application*. New York: CRC Press, 2009.

[3] J. A. Kong, A. A. Swartz, H. A. Yueh, L. M. Novak, and R. T. Shine, "Identification of terrain cover using the optimal terrain classifier," *J. Electromagn. Waves Appl.*, vol. 2, no. 2, pp. 171–194, 1988.

[4] H. A. Yueh, A. A. Schwartz, J. A. Kong, R. T. Shin, and L. M. Novak, "Bayes classification of terrain cover using normalized polarimetric data," *J. Geophys. Res.*, vol. 93, no. B12, pp. 15 261–15 267, 1988.

[5] H. H. Lim, A. A. Swartz, H. A. Yueh, J. A. Kong, R. T. Shin, and J. J. van Zyl, "Classification of earth terrain using polarimetric SAR images," *J. Geophys. Res.*, vol. 94, no. B6, pp. 7049–7057, 1989.

[6] J. J. van Zyl and C. F. Burnette, "Bayesian classification of polarimetric SAR images using adaptive a priori probability," *Int. J. Remote Sens.*, vol. 13, no. 5, pp. 835–840, 1992.

[7] J. S. Lee, M. R. Grunes, and R. Kwok, "Classification of multi-look polarimetric SAR imagery based on complex Wishart distribution," *Int. J. Remote Sens.*, vol. 15, no. 11, pp. 2299–2311, 1994.

[8] N. R. Goodman, "Statistical analysis based on a certain multi-variate complex Gaussian distribution (an introduction)," *Ann. Math. Stat.*, vol. 34, no. 1, pp. 152–177, 1963.

[9] L. Ferro-Famil, E. Pottier, and J. S. Lee, "Unsupervised classification of multifrequency and fully polarimetric SAR images based on H/A/alpha-Wishart classifier," *IEEE Trans. Geosci. Remote Sens.*, vol. 39, no. 11, pp. 2332–2342, Nov. 2001.

[10] L. Ferro-Famil, E. Pottier, and J. S. Lee, "Unsupervised classification and analysis of natural scenes from polarimetric interferometric SAR data," in *Proc. IGARSS*, 2001, pp. 2715–2717.

[11] J. J. van Zyl, "Unsupervised classification of scattering behavior using radar polarimetry data," *IEEE Trans. Geosci. Remote Sens.*, vol. 27, no. 1, pp. 36–45, Jan. 1989.

[12] S. R. Cloude and E. Pottier, "An entropy based classification scheme for land applications of polarimetric SAR," *IEEE Trans. Geosci. Remote Sens.*, vol. 35, no. 1, pp. 68–78, Jan. 1997.

[13] J.-S. Lee, M. R. Grunes, T. L. Ainsworth, L.-J. Du, D. L. Schuler, and S. R. Cloude, "Unsupervised classification using polarimetric decomposition and the complex Wishart classifier," *IEEE Trans. Geosci. Remote Sens.*, vol. 37, no. 5, pp. 2249–2258, Sep. 1999.

[14] E. Pottier and J. S. Lee, "Unsupervised classification scheme of POLSAR images based on the complex Wishart distribution and the H/A/alpha-polarimetric decomposition theorem," in *Proc. 3rd EUSAR Conf.*, May 2000, pp. IV-1081–IV-1084.

[15] J. S. Lee, M. R. Grunes, and E. Pottier, "Unsupervised terrain classification preserving polarimetric scattering characteristics," *IEEE Trans. Geosci. Remote Sens.*, vol. 42, no. 4, pp. 722–731, Apr. 2004.
[16] J. R. Huynen, "Phenomenological theory of radar target," Ph.D. dissertation, Delft Univ. Technol., Delft, The Netherlands, 1970.
[17] S. R. Cloude and E. Pottier, "A review of target decomposition theorems in radar polarimetry," *IEEE Trans. Geosci. Remote Sens.*, vol. 34, no. 2, pp. 498–518, Mar. 1996.
[18] A. Freeman and S. L. Durden, "A three-component scattering model for polarimetric SAR data," *IEEE Trans. Geosci. Remote Sens.*, vol. 36, no. 3, pp. 963–973, May 1998.
[19] M. Arii, J. J. van Zyl, and K. Yunjin, "Adaptive model-based decomposition of polarimetric SAR covariance matrices," *IEEE Trans. Geosci. Remote Sens.*, vol. 49, no. 3, pp. 1104–1113, Mar. 2011.
[20] W. L. Cameron, N. N. Youssef, and L. K. Leung, "Simulated polarimetric signatures of primitive geometrical shapes," *IEEE Trans. Geosci. Remote Sens.*, vol. 34, no. 3, pp. 793–803, May 1996.
[21] D. G. Corr and A. Rodrigues, "Alternative basis matrices for polarimetric decomposition," in *Proc. 3rd EUSAR Conf.*, Cologne, Germany, 2002, pp. 597–600.
[22] T. Moriyama, S. Uratsuka, T. Umehara, H. Maeno, M. Satake, A. Nadai, and K. Nakamura, "Feature extraction of urban area based on polarimetric decomposition," in *Proc. 4th EUSAR Conf.*, Ulm, Germany, 2004, pp. 435–438.
[23] O. Antropov, Y. Rauste, and T. Häme, "Volume scattering modeling in PolSAR decompositions: Study of ALOS PALSAR data over boreal forest," *IEEE Trans. Geosci. Remote Sens.*, vol. 49, no. 10, pp. 3838–3848, Oct. 2011.
[24] Y. Yamaguchi, T. Moriyama, M. Ishido, and H. Yamada, "Four-component scattering model for polarimetric SAR image decomposition," *IEEE Trans. Geosci. Remote Sens.*, vol. 43, no. 8, pp. 1699–1706, Aug. 2005.
[25] Z. Shan, C. Wang, H. Zhang, and W. An, "Improved four-component model-based target decomposition for polarimetric SAR data," *IEEE Geosci. Remote Sens. Lett.*, vol. 9, no. 1, pp. 75–79, Jan. 2012.
[26] J. Yang, Y. N. Peng, Y. Yamaguchi, and H. Yamada, "On Huynen's decomposition of a Kennaugh matrix," *IEEE Geosci. Remote Sens. Lett.*, vol. 3, no. 3, pp. 369–372, Jul. 2006.
[27] J. Yang, Y. N. Peng, and S. M. Lin, "Similarity between two scattering matrices," *Electron. Lett.*, vol. 37, no. 3, pp. 193–194, Feb. 2001.
[28] Q. Chen, Y. M. Jiang, L. J. Zhao, and G. Y. Kuang, "Polarimetric scattering similarity between a random scatterer and a canonical scatterer," *IEEE Geosci. Remote Sens. Lett.*, vol. 7, no. 4, pp. 866–869, Oct. 2010.
[29] J. S. Lee, M. R. Grunes, and G. de Grandi, "Polarimetric SAR speckle filtering and its implication for classification," *IEEE Trans. Geosci. Remote Sens.*, vol. 37, no. 5, pp. 2363–2373, Sep. 1999.

Qiang Chen received the B.Sc. and M.Sc. degrees from the Air Force Radar Institute, Wuhan, China, in 2002 and 2006, respectively, and the Ph.D. degree in remote sensing from the National University of Defense Technology, Changsha, China, in 2010.

He is currently with the School of Electronic Science and Engineering, National University of Defense Technology. He is the first author of over 20 papers and one book. His research interests include synthetic aperture radar (SAR) image processing, polarimetric scattering modeling, supervised/unsupervised polarimetric SAR image classification, and basic theory of polarimetry.

Gangyao Kuang (M'09) received the B.Sc. and M.Sc. degrees from Central South University, Changsha, China, in 1988 and 1991, respectively, and the Ph.D. degree from the National University of Defense Technology, Changsha, in 1995.

Since 1996, he has been a Codirector of the Remote Sensing Information Processing Laboratory, National University of Defense Technology, where he has also been a Professor. In 2009-2010, he was a Visiting Professor with the Laboratory for GeoSpatial Technology and Remote Sensing, Department of Geography and Environmental Management, University of Waterloo, Waterloo, ON, Canada. He is the author of over 200 papers. His current interests include remote sensing, synthetic aperture radar (SAR) image processing, change detection, ground moving target detection, and polarimetric SAR image classification.

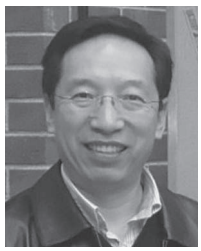

Jonathan Li (M'00–SM'11) received the Ph.D. degree in geomatics engineering from the University of Cape Town, Cape Town, South Africa, in 2000.

He is currently with the Key Laboratory of Underwater Acoustic Communication and Marine Information Technology, Ministry of Education, and the School of Information Science and Engineering, Xiamen University, Xiamen, China, and the Director of the Laboratory for GeoSpatial Technology and Remote Sensing, Department of Geography and Environmental Management, University of Waterloo, Waterloo, ON, Canada, where he is also a Professor. He has coauthored more than 180 publications, over 60 of which were published in refereed journals. His current research interests include synthetic aperture radar image analysis for shoreline and oil spill detection and 3-D surface reconstruction from mobile LiDAR point clouds.

Dr. Li is the Chair of the Inter-Commission Working Group V/I on Land-Based Mobile Mapping Systems of the International Society for Photogrammetry and Remote Sensing (2008–2012), the Vice Chair of the Commission on Hydrography of the Fédération Internationale des Géomètres (2011–2014), and the Vice Chair of the Commission on Mapping from Remote Sensing Imagery of the International Cartographic Association (2011–2015).

Lichun Sui received the B.Eng. degree in photogrammetry from the Zhengzhou University of Information Engineering, Zhengzhou, China, in 1983, the M.Sc. degree in photogrammetry and remote sensing from Wuhan University, Wuhan, China, in 1989, and the Ph.D. degree in photogrammetry and remote sensing from the Technical University of Berlin, Berlin, Germany, in 2000.

He is currently a Professor with the State Key Laboratory of Astronautic Dynamics, Xi'an, China, and the Associate Dean of the School of Geology Engineering and Geomatics, Chang'an University, Xi'an. He has published more than 30 research papers in refereed journals and proceedings. His current research interests include synthetic aperture radar (SAR) image analysis, LiDAR data processing and software development, interferometric SAR, and spatial data mining.

Diangang Li received the B.Sc. degree from the Air Force Radar Institute, Wuhan, China, in 1995.

He currently holds a post in the 93502 Unit, People's Liberation Army, Hohhot, China. His interests include synthetic aperture radar (SAR) image processing, polarimetric scattering modeling, polarimetric SAR image classification, and assessment and training.